Alma Mater Studiorum Università di Bologna
Archivio istituzionale della ricerca

Prediction of gas cavities size and structure and their effect on the power consumption in a gas-liquid stirred tank by means of a two-fluid RANS model

21 July 2024

Prediction of gas cavities size and structure and their effect on the power consumption in a gas-liquid stirred tank by means of a two-fluid RANS model

Francesco Maluta[a]*, Alessandro Paglianti[b], Giuseppina Montante[a]

[a]Dipartimento di Chimica Industriale 'Toso Montanari', Alma Mater Studiorum – Università di Bologna, via Terracini 34, 40131, Bologna, Italy

[b]Dipartimento di Ingegneria Civile, Chimica, Ambientale e dei Materiali, Alma Mater Studiorum – Università di Bologna, via Terracini 34, 40131, Bologna, Italy

* Corresponding author: francesco.maluta@unibo.it

Abstract

Aerated cavities behind the impeller blades in stirred tanks affect the power transferred to the liquid that in turns affects heat and mass transfer, thus the development of fully predictive simulation methods to detect the formation of cavities, their size and structures is of paramount importance for an effective simulation of aerated reactors and bioreactors. In this work, operating conditions corresponding to different cavity structures are investigated by means of a Reynolds averaged two-fluid model without adjustable parameters. Based on the comparison with previous experiments and correlations, the method is proved to be reliable in the prediction of the transition between vortex-clinging and small '3-3' cavities, cavity size and power drawn reduction. For the first time, small '3-3' cavities with volume fractions close to unity are obtained with a steady approach. The power reduction mechanism is observed and a novel interpretation of the formation of the asymmetrical cavities is proposed.

1 Introduction

Gas-liquid stirred tanks are frequently used in many industries such as, for instance, chemical engineering, biotechnology, and mining [1,2]. The numerical simulation of the multiphase fluid dynamics of this equipment is often performed with a Two-Fluid Model (TFM) approach, in the context of the Reynolds Averaged Navier-Stokes (RANS) equations [3], due to the relatively cheap computational demands of this modelling method, that is the only one actually usable at industrial scale and high dispersed phase volume fraction [4]. Besides this common modelling ground, several different correlations are often adopted in the closure of the model equations, depending on the investigated range of operating conditions, bubble size modelling approach, and scale of the interphase phenomena [5]. Furthermore, closure models for turbulent bubbly flows may contain empirical parameters that are often adjusted to match a specific data-set used in the development and testing of a particular modelling approach, thus making it less readily applicable [6]. The predictive Computational Fluid Dynamics (CFD) simulation of gas-liquid stirred tanks has been an active field of study since the late 90's of the last century [7] and a recent review of the state of the art of TFM/RANS modeling of gas-liquid stirred tank was performed by Shi and Rzehak (2020) [5]. By means of example, in this context stirred tanks have been approached in terms of a thorough study of the turbulent features of the gas-liquid flow [5,8], focusing on the local gas hold-up and bubble sizes [9,10], addressing the prediction of the mixing time in the liquid phase [11] and of the interphase mass transfer [12,13].

One of the most important features of the gas-liquid fluid dynamics in mechanically stirred tanks is the reduction of the power drawn by the impeller, due to the formation of gas cavities behind flat impeller blades [14–16]. A gas cavity behind the impeller blades means that segregation exists between the gas and the liquid phase, thus the expected local gas volume fraction should be close to unity. The gas accumulation behind the impeller blades has been qualitatively predicted by several authors, but with local volume fractions of gas that are usually far from the expected values. In particular, many early investigations predicted a gas volume fraction of around 0.15 [17,18]. By means of example, Ranade et al. (2001) [17] predicted a local volume fraction behind the impeller blades larger than 0.1 and advanced the hypothesis that the model was incapable of simulating gas cavity formation since a coalescence model was not included in the formulation,

even though they captured significant gas accumulation in the region of trailing vortices. Kerdouss et al. (2006) [18] modified the drag law to account for the effect of turbulence changing the viscosity term in the relative Reynolds number and obtaining a local volume fraction of 0.1. Other works managed to predict higher local gas accumulation behind the impeller blades with values up to 0.3 [19,20] in operating conditions where the '3-3' cavity structures were expected. Despite the larger gas accumulation, no asymmetry was observable from their results. Local gas hold-up of 0.5 was predicted by Kshatriya et al. (2007) [21] and by Deen et al. (2002) [22] and the authors reported that continuous and dispersed volume fraction was used in their formulation of the drag force. Experimental studies on swarms of bubbles in bubble columns [23] lead to the formulation of a drag law in which it was included the dispersed phase volume fraction and this formulation proved successfully in the numerical prediction of regime transitions in bubble columns [24]. The inclusion of the continuous and disperse phase volume fractions in the drag force imposes that the interphase forces go to zero when high volume fractions of continuous and dispersed phases are locally found. In the simulation of stirred tanks, this was accounted for by Lane et al. (2005) [9] modifying the bubble diameters at high gas hold ups by means of an algebraic function dependent on an adjustable parameter. The modified bubble diameter thus produced a modified drag coefficient. With this approach, the authors predicted a local gas volume fraction of 0.8. In a recent publication Cappello et al. (2021) [4] obtained aerated gas cavities with gas volume fractions up to 1 with TFM-RANS simulations with a Multiple Reference Frame and with a Sliding Mesh description of the impeller motion. In the latter case, the authors predicted the '3-3' cavity structures, while with the former approach that was not observed, even because just one sixth of the geometry was simulated. More recently, the promising capability of a fully predictive methodology based on the TFM-RANS model for the simulation a multiple impeller gas-liquid stirred tank for industrial fermentation application, including the gas cavities formation, has been presented [25]. Overall, further analysis of the modelling techniques and fully predictive methodology as well as experimental validation of the results in a wide range of gas-liquid dispersion conditions are required for assessing the reliability of RANS based simulation of gas-liquid stirred tanks, particularly when gas accumulation takes place, due to the power draw reduction and its important effect on the volumetric mass transfer coefficient.

In this study, the computational method advanced in a previous investigation [25] is applied to a single impeller stirred tank under different operating conditions, corresponding to a single gas-

liquid flow regime of incomplete recirculation (loading conditions) and different cavity structures, namely the vortex-clinging and the '3-3' small cavities. The goal of the study is to provide a severe benchmark for the model by the comparison of predictions with previously published experimental data, in terms of both cavity size and gassed to ungassed power ratio by adopting a fully predictive methodology.

2   Stirred tank operating conditions

Different gas flow rates, Q_G, at the same impeller rotational speed N, were selected to investigate the gas cavity formation behind the blade of the impeller, in the loading flow regime of a standard geometry stirred tank. The gas cavity area formed at the rear of the blades of a Rushton and the relative power demand (RPD), experimentally obtained by Paglianti et al. (2008) [26] in a tank of diameter equal to 0.48m stirred with a Rushton impeller of diameter equal to 0.151m positioned at an off-bottom clearance of 0.24m, were adopted to quantitatively validate the numerical results presented in terms on non-dimensional quantities, for a direct comparison, with the smaller stirred tank simulated in this work. The investigated operating conditions [26] are reported in Figure 1 in a map obtained with correlations from the literature for the identification of the gas cavity structures as a function of relevant dimensionless numbers, that are the Froude, $Fr = N^2 D/\boldsymbol{g}$, and the gas flow number, $Fl_G = Q_G/D^3 N$, with D being the impeller diameter and $\boldsymbol{g}$ being the gravitational acceleration.
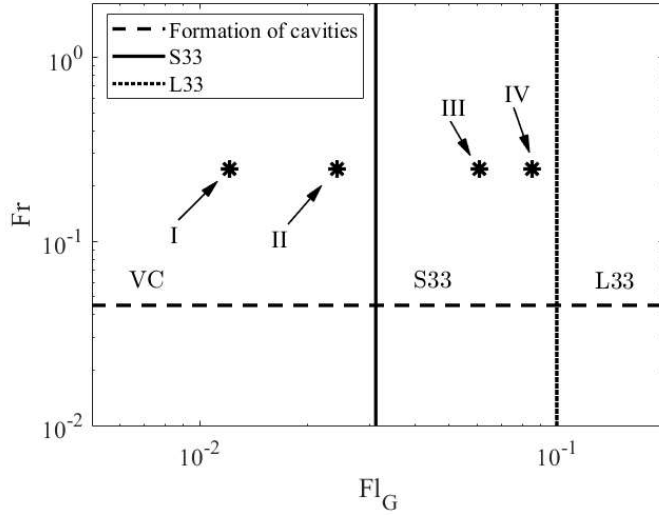
Figure 1 – Gas cavities map obtained from Eqs. 1-3. The symbols represent the investigated operating conditions.

The condition at which cavities develop is obtained from [14]:

$$(Fr)_{CD} = 0.045 \qquad\qquad 1$$

With $(Fr)_{CD}$ being the minimum Froude number at which cavities are observed. The transition from vortex and clinging cavities to small '3-3' cavity structure (S33), that corresponds to 3 large and 3 clinging cavities, occurs at [14]:

$$(Fl_G)_{3-3} = 0.0038 \left(\frac{Re^2}{Fr}\right)^{0.07} \left(\frac{T}{D}\right)^{0.5} \qquad\qquad 2$$

Where $(Fl_G)_{3-3}$ is the impeller gas flow number at which the transition is observed, and $Re = ND^2\rho_L/\mu_L$ is the impeller Reynolds number. Small '3-3' cavities are expected up to [14]:

$$Fl_G = 0.1 \qquad\qquad 3$$

in fact, at gas flow numbers higher than this threshold large '3-3' cavities develop (L33), consisting in 3 small and 3 large alternating cavities.

The four operating conditions investigated by means of computational fluid dynamics indicated with Roman numerals in Figure 1 were chosen in order to assess the general applicability of the modelling approach, thus covering different conditions. According to the correlations from the literature, shown in Figure 1, Cases I and II develop vortex-clinging cavities, while in Cases III and IV small '3-3' cavities are expected. As in the experiments, the gas-liquid system consisted of

5

water (density ρ_L=998 kg/m^3 and viscosity μ_L=0.001 Pa·s) and air (density ρ_G=1.2 kg/m^3). The gas flow rate, the relative impeller gas flow number, the Froude number, and the gas superficial velocity $U_{sup} = Q_G/(T^2\,\pi/4)$ corresponding to each case are summarized in Table 1. The simulations were run in the computational domain that closely matched the geometry of a standard geometry stirred tank reproducing a scale down by a factor of 0.48 of the one used by Paglianti et al. (2008) [26]. A cylindrical, flat-bottomed, fully baffled stirred tank with diameter, T, of 0.23m, with four equally spaced baffles T/10 wide and a Rushton impeller of diameter, D, equal to T/3, with an off-bottom clearance of T/2 mounted on a central shaft was adopted. The liquid height is equal to T and the gas is injected in the system through a ring sparger of diameter 0.4D positioned at an off-bottom axial distance of T/5. As for the gas dispersion condition, following the correlations developed by Nienow [16,27,28], the loading flow regime is expected for all the Cases.

Table 1 – Operating conditions of the different cases considered in this work, N=5.6s^{-1}

Case Number	Q_G – [L/h]	Fl_G	Fr	U_{sup} – [m/s]	P_g/P_u
I	110	0.012	0.25	0.7×10^{-3}	0.88
II	221	0.024	0.25	1.5×10^{-3}	0.75
III	554	0.061	0.25	3.7×10^{-3}	0.54
IV	775	0.085	0.25	5.2×10^{-3}	0.43

The gassed to ungassed power consumption ratio reported in Table 1, that will be adopted for the estimation of the bubble size, was obtained with the following approach proposed by Smith et al. [29], which estimates the gassed to ungassed power ratio based on the gas-liquid flow regime and the cavity structures.

When there is formation of vortex-clinging cavities, the relative power demand is calculated as:

$$\frac{P_g}{P_u} = 1 - 16.7(Fl_G)(Fr)^{0.35} \qquad\qquad 4$$

While with small '3-3' cavities the relative power demand is obtained from:

$$\frac{P_g}{P_u} = B + (A - B)\frac{Fl_G - 0.1}{(Fl_G)_{3-3} - 0.1}$$

$$A = 1 - 17(Fl_G)_{3-3}(Fr)^{0.35} \qquad\qquad 5$$

$$B = 0.27 + 0.022/Fr$$

3   Model description

The modelling approach is based on the steady state Reynolds averaged formulation of the Two-Fluid model equations, namely the Eulerian multifluid model as implemented in ANSYS Fluent 19.3, that reads as:

$$\nabla \cdot (\alpha_i \rho_i \boldsymbol{u}_i) = 0 \tag{6}$$

$$\nabla \cdot (\alpha_i \rho_i \boldsymbol{u}_i \boldsymbol{u}_i) = -\alpha_i \nabla P + \alpha_i \rho_i \boldsymbol{g} + \nabla \cdot (\boldsymbol{\tau}_i + \boldsymbol{\tau}_i^t) + \boldsymbol{F}_D + \boldsymbol{F}_{TD} \tag{7}$$

With α_i being the volume fraction of the phase i, ρ_i its density, $\boldsymbol{u}_i$ the mean velocity vector of the phase i, $\boldsymbol{\tau}_i$ and $\boldsymbol{\tau}_i^t$ its laminar viscous stress tensor and the Reynolds stress tensor respectively, P being the pressure. The standard k-ε turbulence model, considering phase-averaged properties (mixture formulation) as implemented in the ANSYS Fluent 19.3 CFD software, was used to calculate the Reynolds stress tensor.

The momentum conservation equations for the liquid and gas phase are coupled through two interphase momentum exchange terms, namely the drag force, $\boldsymbol{F}_D$, and the turbulent dispersion force, $\boldsymbol{F}_{TD}$. Based on previous results, additional contributions to the interphase momentum transfer are neglected [10,13,19].

The drag force was expressed in terms of the bubble terminal velocity by a User Defined Function (UDF), as:

$$\boldsymbol{F}_D = \frac{\alpha_L \alpha_G}{U_t^2} \boldsymbol{g} (\rho_L - \rho_G) \|\boldsymbol{u}_G - \boldsymbol{u}_L\| (\boldsymbol{u}_G - \boldsymbol{u}_L) \tag{8}$$

Where $\boldsymbol{u}_G$ and $\boldsymbol{u}_L$ are the gas and the liquid mean velocities respectively, ρ_L and ρ_G are the liquid and gas densities, and U_t is the bubble terminal velocity. In Eq.8 both the disperse and continuous phase volume fractions are present, and the latter is due to the force balance performed in a Eulerian frame [23], as already done for swarms of bubbles in bubble columns [24].

The Burns et al. [30] model was adopted to describe the turbulent dispersion force, adopting the bubble terminal velocity, as in the drag force, as:

$$\boldsymbol{F}_{TD} = \frac{\alpha_L \alpha_G}{U_t^2} \boldsymbol{g} (\rho_L - \rho_G) \|\boldsymbol{u}_G - \boldsymbol{u}_L\| \left[\frac{\mu_t}{\rho_L Sc_{t,L}} \left(\frac{\nabla \alpha_G}{\alpha_G} - \frac{\nabla \alpha_L}{\alpha_L} \right) \right] \tag{9}$$

Where μ_t is the turbulent viscosity and $Sc_{t,L}$ is the turbulent Schmidt number for the liquid phase, with a default value of 0.9. As already pointed out by Scargiali et al. [31], the advantage of adopting the bubble terminal velocity instead of the bubble drag coefficient in Eq. 8 and 9 is to directly adopt the sole parameter really characterizing the interphase momentum exchange. It is particularly convenient in gas-liquid dispersions, since, depending on the conditions, slight variations of the bubble terminal velocity are obtained in certain bubble size ranges, thus leading to the same results whether a single bubble size or a bubble size distribution were employed to model the disperse phase.

The bubble terminal velocity is obtained with the correlation by Grace et al. (2005) [32], that reads:

$$U_t = \frac{\mu_L}{\rho_L d_B} Mo^{-0.149} \left(C_1 \left[\frac{4}{3} Eo\, Mo^{-0.149} \right]^{\beta} - 0.857 \right) \qquad\qquad 10$$

Where $Mo = \mu_L^4 \boldsymbol{g}(\rho_L - \rho_G)/(\rho_L^2 \sigma^3)$ is the Morton number equal to 2.6×10^{-11}, in which μ_L is the liquid viscosity, and $Eo = \boldsymbol{g}(\rho_L - \rho_G)d_B^2/\sigma$ is the Eötvös number, reported in Table 2, with σ being the water surface tension equal to 0.072 N/m. The constant bubble diameter, d_B, is obtained from established correlations from the literature [33], as treated in detail in Section 3.1. When the term in square brackets is between 2 and 59.3, C_1 and β are equal to 0.94 and 0.757 respectively, while when the term in square brackets is bigger than 59.3, C_1 and β are equal to 3.42 and 0.441 respectively. The correlation by Grace et al. (2005) [32], applies to the ellipsoidal bubbles expected in the investigated flow regime. When the bubble Reynolds numbers, $Re_B = U_t \rho_L d_B / mu_L$ reported in Table 2, assumes values $0.1 < Re_B < 300$, deviations from a spherical shape and internal circulation are so small that the correlations for spherical bubbles and elliptical bubbles predict very similar terminal velocities [32]. For spherical bubble Reynolds number up to 400, the deviation between the terminal velocity obtained with the Schiller and Naumann correlation [34] and the Grace et al. (2005) [32] correlation is less than 5%.

3.1 Bubble size correlations

The correlations derived by Alves et al. (2002) [33] were adopted to obtain the bubble size either in the bulk of the tank or at the turbine discharge. In the work by Paglianti et al. (2008) [26] a coalescent liquid was used (de-ionized water), therefore Eq.11, that describes the Sauter mean bubble diameter in the bulk of stirred tanks with coalescing continuous phase, was adopted:

$$d_B = 0.0076 \left(\frac{P_g}{V}\right)^{-0.14}$$ *11*

For the Sauter mean bubble diameter in the impeller zone, Alves et al. (2002) [33] report two different correlations. For U_{sup} lower than 2×10^{-3}, such as Cases I and II in this study, Alves et al. (2002) [33] report that for both coalescing and non coalescing systems the Sauter mean bubble diameter can be correlated with the following single expression:

$$d_B = 0.25 \left(\frac{P_g}{V_I}\right)^{-0.52}$$ *12*

while for U_{sup} higher than the above-mentioned threshold (Cases III and IV), when the effect of the gas loading becomes important, the correlation for the Sauter mean bubble diameter in the impeller zone for coalescing systems becomes:

$$d_B = 8.5 \left(1 + 32.5\frac{Q}{D^2}\right)\left(\frac{P_g}{V_I}\right)^{-0.24}$$ *13*

In Eq.11-13, P_g is the impeller power consumption in gassed conditions, obtained from Eq. 4-5, V is the volume of the mixture in the tank and V_I is the volume swept by the impeller, that for the Rushton turbine is equal to $V_I = \pi/20\,D^3$.

The bubble diameters obtained with Eq.11-13 are reported in Table 2, together with the terminal velocities as obtained with Eq.10. As can be observed in Table 2, the terminal velocities of the bubbles are identical for the bulk Sauter mean diameter range considered in this study. In these conditions the shape of the bubbles is ellipsoidal, and it is known that the terminal velocity of bubbles in the ellipsoidal regimes is almost unvarying in a wide size range.

Table 2 – Bubble diameters and terminal velocities for the different Cases

Case Number	Bulk (Eq.11)				Impeller (Eq.12 -13)			
	d_B - [mm]	U_t –[m/s]	Re_B	Eo	d_B - [mm]	U_t –[m/s]	Re_B	Eo
I	3.6	0.25	889	1.74	1.2	0.14	164	0.19
II	3.7	0.25	906	1.82	1.3	0.15	190	0.23
III	3.8	0.25	946	2.00	1.5	0.16	245	0.31
IV	4.0	0.25	974	2.13	1.9	0.19	357	0.48

Moreover, the predicted bubble diameter shows just small differences in the four Cases. Table 2 also shows that the range of terminal velocities of the bubbles with the Sauter mean diameter as

obtained with correlations in the impeller zone barely changes, the only exception being Case IV, for which the bubble terminal velocity is higher since the bubble regime is transitioning from spherical to ellipsoidal.

4   Computational domain and solution procedure

The computational domain is shown in Figure 2, and it was discretized in about 2 million hexahedral cells, that are sufficient to produce grid independent mean flow and turbulent variables [35].
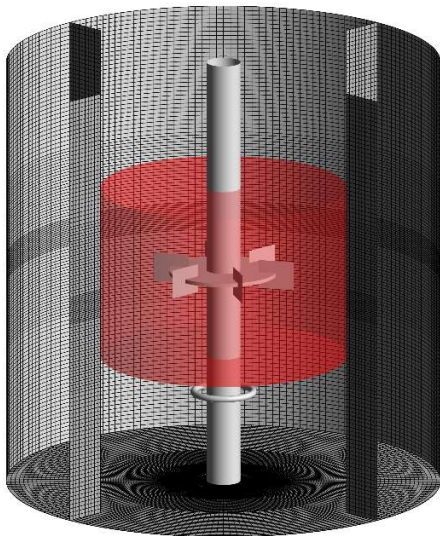

Figure 2 – Stirred tank meshed geometry. The interface between rotating and stationary reference frame is highlighted in red.

The relative motion of the rotating impeller and the tank wall and baffles was modelled with the so-called multiple reference frame, MRF, algorithm. The stirred tank volume was divided into 2 different domains: one for the cells in the proximity of the impeller and one for the remaining cells. For both phases no-slip boundary conditions were adopted at the solid walls.

A single-phase velocity inlet was assumed for the gas phase on the upper surface of the air-sparger and the so-called degassing boundary condition was adopted on the free surface at the top of the tank, acting as an outflow boundary condition for the gas phase and as a free-slip wall for the liquid phase. The free surface was always located at an elevation equal to T, since for the investigated conditions the maximum expected variation of the liquid height due to the gas entrainment was less than 5 mm.

The momentum and the transport of turbulent variables equations were discretized with the second order upwind scheme, while for the volume fraction transport equation the QUICK scheme was used. The pressure-based coupled algorithm as implemented in ANSYS Fluent was adopted for the pressure-velocity coupling. The single-phase steady state flow field was used as the initial conditions for the simulations. Air was then injected from the sparger and the two-phase steady state solution was achieved by means of a pseudo-transient approach [36] with pseudo-time-steps of 0.001s. Since steady-state MRF TFM simulations in Fluent do not enforce mass conservation, this approach was necessary to ensure it. The iterative solution was stopped after the scaled residuals reached constant values of the order of 10^{-5} - 10^{-6}, after the forces measured on the impeller blades and the baffles reached a constant value and when the mass flux injected from the sparger matched the net mass flux exiting the system, ensuring a negligible mass imbalance.

5   Results and discussion

The results of the CFD simulations are presented in this section. Firstly, the predictions in different cavity regimes are analysed, with particular focus on the different cavity structures and the subsequent relative power demands. Then, the effect of the bubble size obtained from the correlations on the gassed to ungassed power ratio and on the cavity size and shape is treated. Lastly, the power draw reduction due to the presence of the gas cavities is assessed through a local analysis of the pressure field on the two sides of the impeller blades and through the analysis of the liquid flux pumped by the impeller.

5.1   Predictions of different cavity structures

Case I to IV were simulated to assess the gas cavity predictions and the relative reduction in the power consumption for different cavity structures in the loading regime. In these simulations, a single Sauter mean bubble diameter in the impeller zone, $d_{Impeller}$, was adopted for each simulation to calculate the bubble terminal velocity in the whole vessel.

The cavities were defined as the grid cells in which the gas volume fraction is higher than 0.95 and they are presented in Figure 3 for all the four Cases. Figure 3 shows that the present model

can predict the cavity shape. In Case I and II vortex-clinging cavities are expected, while determining the relative weight of the vortex and the clinging contribution to the aerated cavity may prove challenging. Experimental observations of Van't Riet & Smith [37] report that in their system just vortex cavities developed at Fr = 0.0845 and Fl_G = 0.0067 and increasing the gas flow rate results in the whole rear surface of each blade carrying a clinging cavity. The clinging cavities in Case I, Figure 3 (a), and Case II, Figure 3 (b), are predicted by the model with bigger size at higher gas flow rates, as expected. The shape of the vortex-clinging cavities, as reported in the literature [16], exhibits also two "elongations" corresponding to the trailing vortexes. This feature is not predicted in the numerical simulations since the Reynolds Averaged formulation of the Navier-Stokes equations is intrinsically ineffective in predicting the trailing vortexes that originate behind the impeller blades.
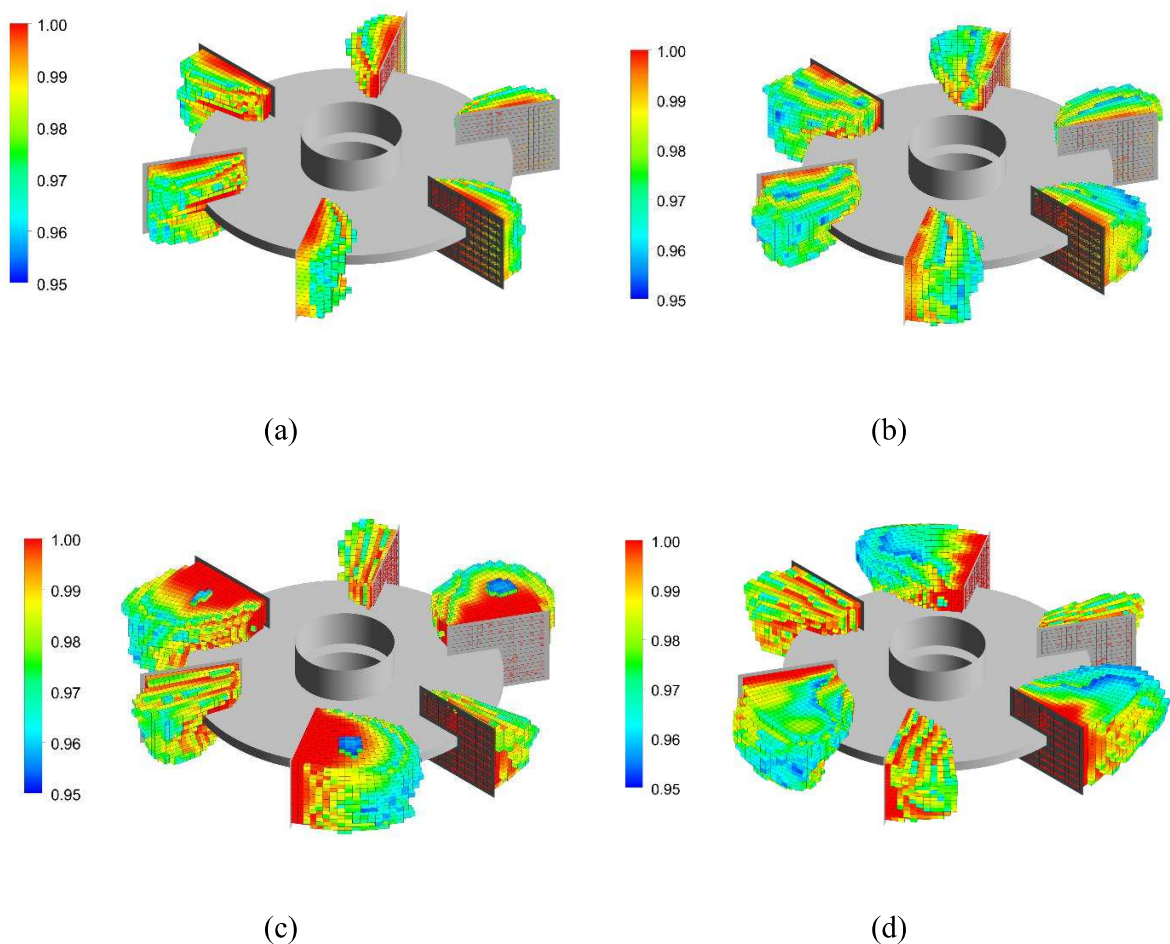

(a)   (b)

(c)   (d)

Figure 3 - Gas cavities as predicted for Case I (a), Case II (b), Case III (c) and Case IV (d). The color map indicates the gas volume fraction.

12

The small '3-3' structures of Case III and IV are visible in Figure 3 (c) and (d) respectively, and the alternation of large and clinging cavities is consistently captured by the simulations. In previous publications [17] it was speculated that the numerical prediction of the gas cavities required the inclusion of a coalescence mechanism in the model. It is worth to underline that in this work the prediction of cavities with high gas volume fraction (higher than 0.95) was captured without including any coalescence model. Moreover, alternating pattern of the small '3-3' cavities was obtained with a steady-state MRF simulation and, to the best of authors' knowledge, this is the first time that this feature has been successfully reproduced in this context.

A quantitative comparison between the cavity to impeller area ratio numerically predicted and experimentally measured by Paglianti et al. (2008) [26] is shown in Figure 4. For a direct comparison with the experimental values, that were obtained from bottom pictures of the cavities, the surfaces enveloping the cavities are projected on a plane parallel to the bottom of the tank and the total projected area is divided by the area swept by the impeller.
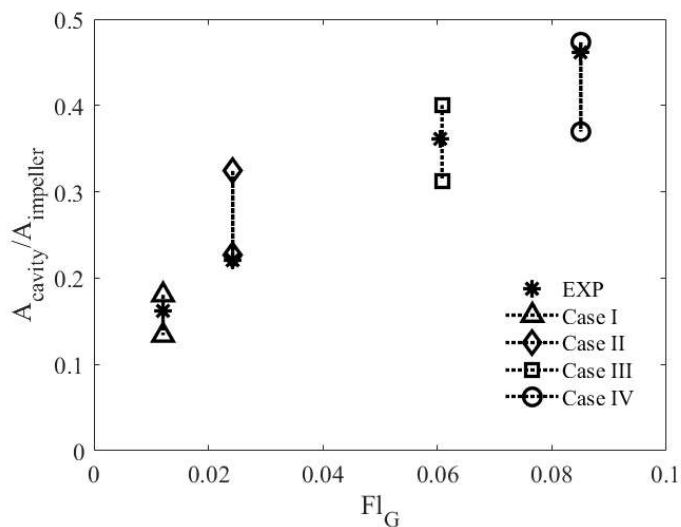

Figure 4 – Comparison between experimental (Exp.) [26] and the CFD prediction of the cavity area to impeller area ratio for the different Cases as a function of the gas flow number.

The exact value of the gas volume fraction defining the cavity is not known, but it would be close to unity. This uncertainty affects both the experimental and the numerical results, hence two values of the gas volume fraction of the cavities were used, to assess the sensitivity of the results on this choice.

The two values were computed considering the cavity as a volume where the gas volume fraction is higher than 0.95 (higher value) or with gas volume fraction higher than 0.99 (lower value). An overall good agreement between experimental and predicted values is obtained for all cases, with a different level of uncertainty depending on the specific case and the threshold value of the cavity detection.

To quantitatively estimate the capability of the model to catch the experimentally observed cavities, the projected area of the cavity obtained with a gas volume fraction threshold of 0.95 behind each blade was calculated for each Case. The coefficient of variation (CoV) obtained from the standard deviation from the average cavity size was calculated and it was found that the CoV for Case I and Case II is 1.4% and 1.7%, respectively, whereas for Case III and Case IV it is 43.6% and 38.12%, respectively. This result highlights how the cavities have almost the same size in the vortex-clinging regime, whereas large differences are found when the small '3-3' cavities develop. In particular, one large cavity on average contributes to the total projected area of the gas cavities for 23.2% and 22.5%, for Case III and IV respectively, while the area of each small cavity contributes to 10.1% and 10.9% for Case III and IV to the total projected area. This result quantifies the asymmetry observed in the small '3-3' cavity regimes and can be used to estimate the relative size of the cavities for the '3-3' structures.

The simulations also showed the typical shape of the "gas fingers" in the gas pocket below the impeller disk, reported by Warmoeskerken (1986) [38], and they are shown in Figure 5.
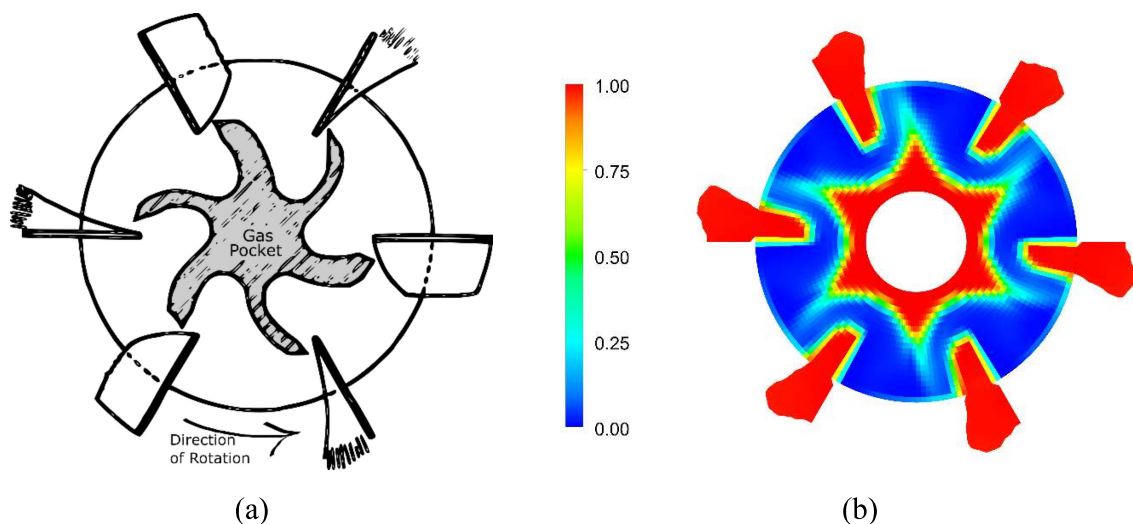

(a)   (b)

The gassed to ungassed power consumption ratio as predicted by the numerical simulations is reported in Figure 6, together with the experimental gassed to ungassed power consumption ratio measured by Paglianti et al. (2008) [26]. The numerical RPD is calculated from the power consumption obtained from the torque on the rotating walls and from the mass integral of the turbulent dissipation rate in the whole tank.
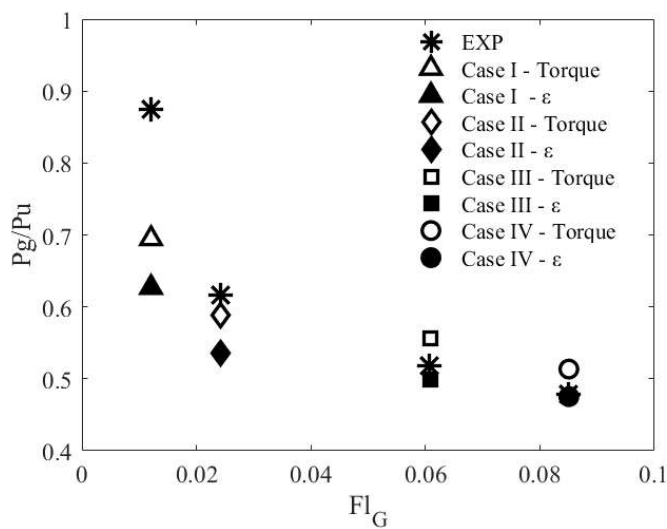

Figure 6 - Comparison between experimental (Exp.) [26] and the CFD prediction of the gassed to ungassed power consumption ratio for the different Cases as a function of the gas flow number. Power consumption is obtained either from the torque on the moving walls or from the integral of the turbulent dissipation rate.

Figure 6 shows that an overall fair agreement is obtained between numerical and experimental results, especially for gas flow numbers higher than 0.02. The RPD from the torque on the rotating walls predicted in Case I is underestimated by 20% with respect to the experimental result, while in the other Cases the average numerical deviation from the experimental results is less than 6.5%. The RPD curve at flow numbers lower than 0.02 shows a steep slope, meaning that small variations of the flow numbers trigger large variations of the RPD. This aspect may be responsible for the worse agreement between numerical and experimental data in these conditions. The RPD obtained from the integral of the turbulent dissipation rate shows the same trend as the RPD from the torque on the rotating walls. The systematic deviation between the two computed RTD values may be due to the multiphase formulation of the turbulence model that was used in this work, that uses

averaged values in the transport equations of the turbulent dissipation rate and the turbulent kinetic energy.

The impeller pumping numbers, for the liquid, $N_{Q,L} = Q_L/ND^3$, and the gas, $N_{Q,G} = Q_G/ND^3$ phases are shown in Figure 7. The liquid and gas flow rates, Q_L and Q_G, were obtained by integrating the phasic radial velocity through the cylindrical surface of diameter 0.34T and height 0.42D enveloping the impeller.

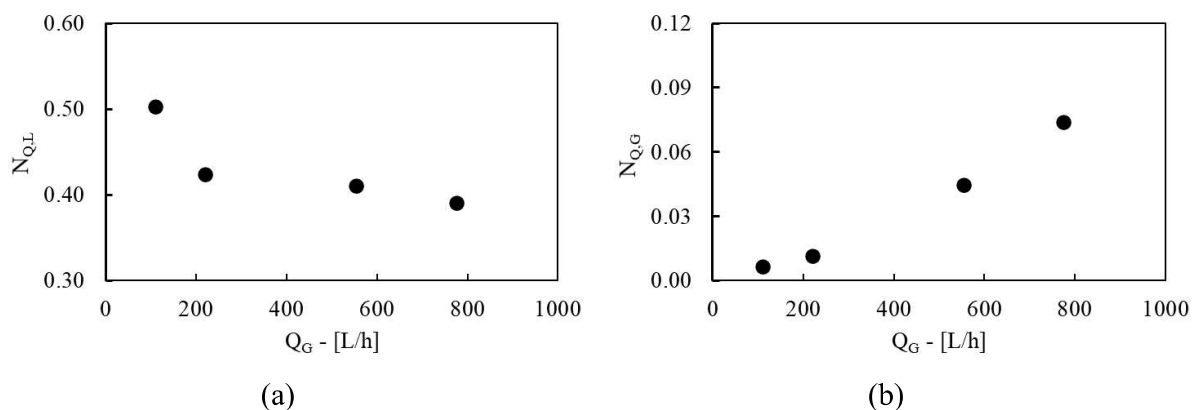

(a)   (b)

Figure 7 – Liquid (a) and Gas (b) impeller pumping numbers as a function of the gas flow rate from the sparger.

Figure 7 (a) shows that $N_{Q,L}$ is in all cases lower than the single phase value of about 0.75 and it is lower at higher gas flow rates. This is expected and consistent with the decrease in the gassed to ungassed power ratio observed in the simulations. The gas pumping number, conversely increases monotonically with the gas flow rate. More gas entering the impeller zone would mean more gas radially discharged by the impeller. On the other hand, as the gas flow rate increases, fraction of the gas entering the lower side of the impeller leaves through the upper part of the impeller, and the turbine cannot direct the totality of the gas in the radial jet. This phenomenon is worsened by the formation of the cavities, which decreases the power transferred to the mixture.

5.2   Effect of the bubble size

In this section the comparison of the results obtained with the bubble diameter in the bulk of the tank, d_{Bulk}, and in the impeller zone, $d_{Impeller}$, is discussed.

The cavities obtained with d_{Bulk} are shown in Figure 8. Just one result in the vortex-clinging cavity regime and one in the '3-3' small cavity regime is shown, for brevity. In Figure 8 the cavities are identified as those cells in which the gas volume fraction is higher than 0.95. Case I and Case

II correspond to a flow regime in which vortex-clinging cavities are expected, but the simulations with the bubble size in the bulk of the tank predict small '3-3' cavities. Small '3-3' cavities are correctly predicted for Case III and Case IV, but the cavities are much larger than those obtained with $d_{Impeller}$, as it can be seen from a comparison with Figure 3 (c).
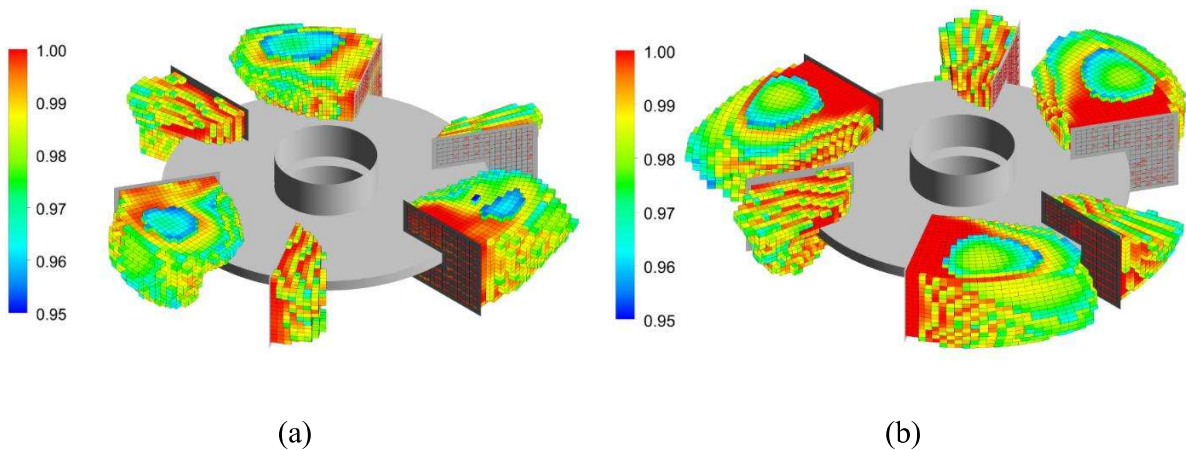

(a)   (b)

Figure 8 - Gas cavities as predicted with the simulations with constant bubble diameter of d_{Bulk} *for Case II (a) and Case III (b). The color map indicates the gas volume fraction.*

A quantitative comparison between the cavity predictions using the two different bubble diameters is shown in Figure 9. The predicted cavity to impeller area ratio obtained with $d_{Impeller}$ and d_{Bulk} in all the operating conditions considered in this work are plotted in a parity plot against the experimental results by Paglianti et al. (2008) [26].
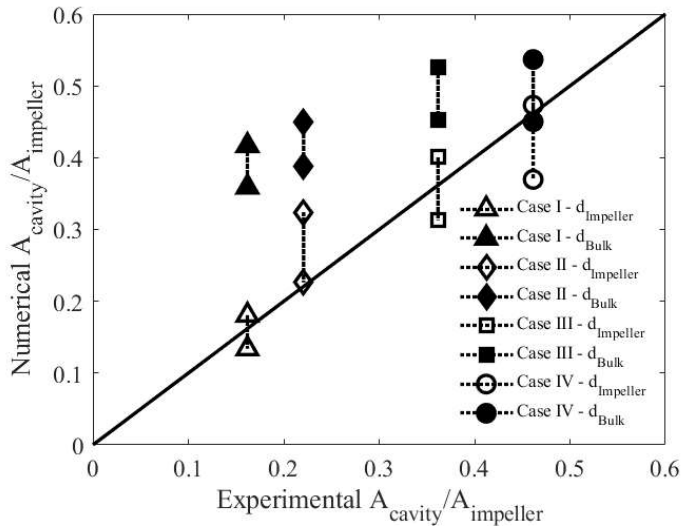
Figure 9 shows that the cavity sizes predicted by the simulations with d_{Bulk} are larger than the cavities obtained with $d_{Impeller}$. For Case I and Case II the cavity to impeller area ratio obtained with d_{Bulk} is 115% larger than the experimental value, while the deviation obtained with $d_{Impeller}$ is 19.6%. For Case III and Case IV, the cavity to impeller area ratio obtained with d_{Bulk} is 22.6% larger than the experimental value, while the deviation obtained with $d_{Impeller}$ is 11.7%. The larger deviation between the predictions with the two different diameters observed in the vortex-clinging regime with respect to the small '3-3' cavity regime is due to the differences in the terminal velocities obtained with the two diameters. In fact, differences between the terminal velocities obtained with d_{Bulk} and $d_{Impeller}$ are larger for Case I and Case II with respect to Case III and Case IV, determining changes in the intensity of the drag and turbulent dispersion forces [25]. It is interesting to notice that for the cavities obtained with $d_{Impeller}$ the deviation is negative for the cavities identified through the gas volume fraction threshold value of 0.99 and positive for the cavities identified with a threshold value of 0.95, suggesting that the experimentally detected threshold value would lie somewhere in between these two values.

The gassed to ungassed power consumption ratio as predicted by the numerical simulations with d_{Bulk} and $d_{Impeller}$ is reported in Figure 10, in a parity plot against the experimental results by Paglianti et al. (2008) [26].
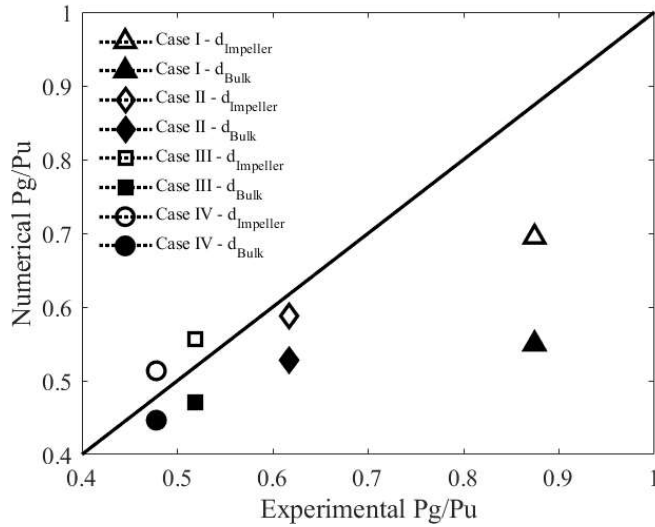
Figure 10 - Parity plot comparing the numerical gassed to ungassed power ratio, obtained by considering $d_{Impeller}$ *and* d_{Bulk}, *and the experimental gassed to ungassed power ratio*.

The numerical power consumption is obtained from the total torque on the rotating walls. Figure 10 shows that the RPD predicted using the bubble size in the bulk of the tank is smaller than the RPD predicted using the bubble size in the impeller zone, consistently with the results on the cavity size. As can be observed, the RPD obtained with the impeller bubble size have an overall better agreement with the experimental data with respect to the results obtained with the bulk bubble size. In particular, using $d_{Impeller}$ as the bubble size, an average underestimation of 12.6% from the experimental data was observed for Case I and Case II, whereas using d_{Bulk} the average underestimation is 25.8%. It is worth underlying that very similar deviations from the experimental value are obtained in Case III and Case IV, with an overestimation of 7.3% and an underestimation of 7.9% with the adoption of $d_{Impeller}$ and d_{Bulk} respectively.

The results presented in this Section indicate that a closer agreement with the experimental data is observed with the adoption of the bubble size as obtained from literature correlations developed to predict the bubble diameter in the impeller zone instead of that developed for the bulk.

5.3 Analysis of the power reduction mechanism

In order to investigate the mechanisms that lead to a power consumption reduction when gas cavities develop, the pressure field in the trailing and leading blade space was analyzed. Four different points (probes) laying on a plane passing through the middle of the impeller disk were selected, in the front and in the back of two opposite blades, as shown in Figure 11 for Case III.
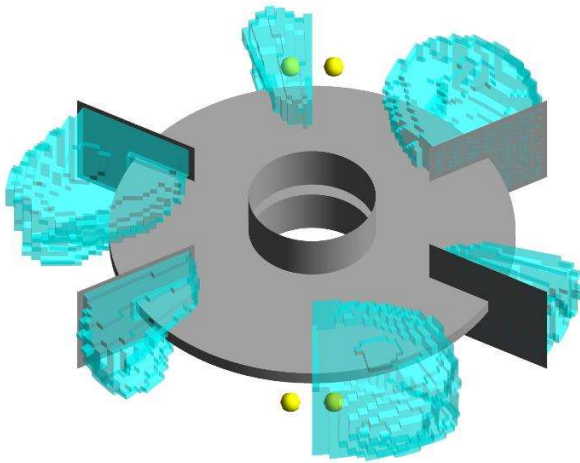
19

Figure 11 – Position of the pressure probes (yellow points) with respect to the blades and the cavities position for Case III.

The points were positioned at a distance of 3mm from two opposite blades, referred to as B1 and B4, so that when small '3-3' structures develop, the probes in the trailing position lay inside a clinging and a large cavity respectively. The pressure measured by the probes was divided by $0.5\rho_L U_{tip}{}^2$, with the impeller tip speed $U_{tip} = \pi ND$, to obtain a non-dimensional relative pressure value. The value obtained in single phase conditions (Q_G=0) is also shown for comparison.

In Figure 12 the non-dimensional relative pressure measured on the probes in the trailing position of the B1 and B4 blades is shown as a function of the inlet gas flow rate.
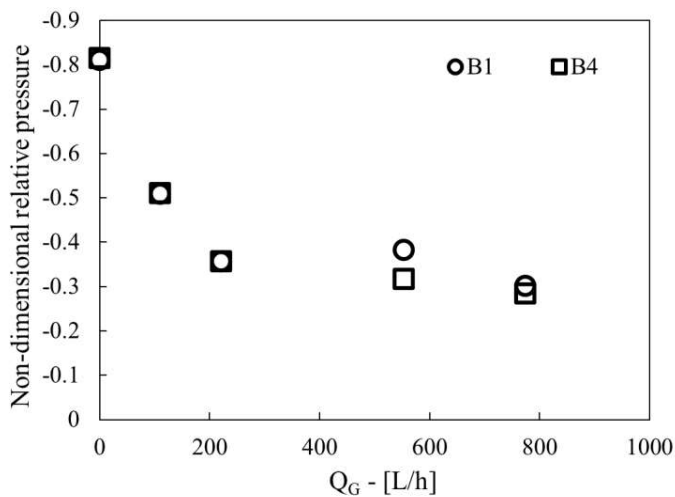

Figure 12 – Non-dimensional pressure as a function of the inlet gas flow rate. The values are obtained in the trailing position of the B1 and B4 blades.

Where cavities develop, the absolute value of the pressure inside the cavities weakly and progressively decreases with the increasing gas flow rate. The same value is obtained with the two probes for single phase and VC structure, while weak differences can be observed in the '3-3' structure cases. The sign of the relative pressure depends on the point chosen as the reference point (in this study it is positioned on the top of the tank, close to the shaft), but this not entails a lack of generality, being the location of the reference in the same position for each Case, being the fluids incompressible and having considered the differential pressure in the calculation of the forces acting on the impeller blades.

Figure 13 shows the non-dimensional pressure measured on the probes in the leading positions of the B1 and B4 blades as a function of the inlet gas flow rate.
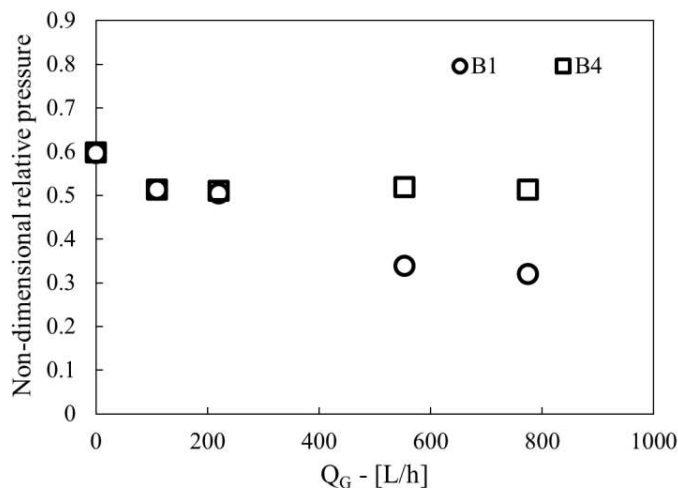

Figure 13 - Non-dimensional pressure as a function of the inlet gas flow rate. The values are obtained in the leading position of the B1 and B4 blades.

The pressure measured in front of the blades is rather constant in the VC cavity regime (Case I and II) and it is close to the single-phase value. In the cases of '3-3' structures, conversely, the pressure in front of a blade on which a large cavity forms, B4, is almost equal to the pressure observed in single-phase and VC regime, while for small cavities, B1, it decreases sharply.

Figure 14 shows the pressure difference between the probes in the leading and trailing position of the blade, that quantifies the resistance faced by the blade. In all cases, the pressure difference decreases at increasing gas flow rate, that results in the power draw reduction discussed above. In the Cases III and IV the presence of large cavities reduces the amount of liquid in the space

between two consecutive blades, thus reducing the amount of pumped liquid. Consequently, the resistance faced by the blade is reduced and the impeller draws less power from the shaft. The reduced power consumption observed with the formation of the cavities is hence due to a reduced pressure in front of the blades and this reduction increases with the cavity size. The power reduction mechanism was already described in the literature [39] and these results quantitatively confirm the power reduction mechanism described by the pioneers in the field.
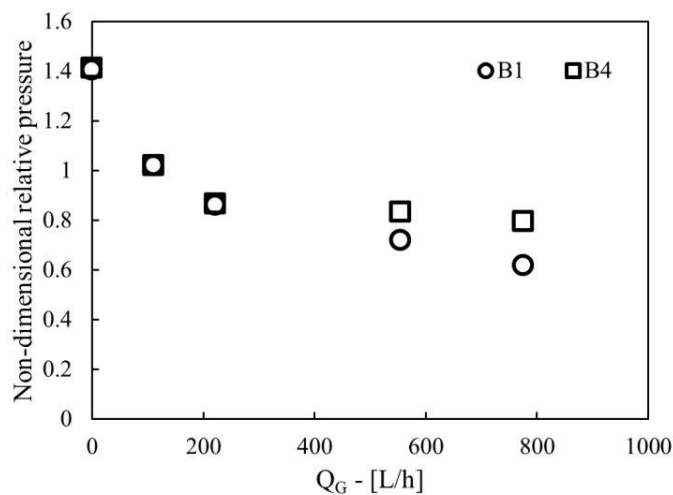

Figure 14 - Non-dimensional pressure difference as a function of the inlet gas flow rate for all the Cases. The values are obtained from the difference between the pressure in the leading and in the trailing position of the B1 and B4 blades.

The further pressure drop observed with the formation of small '3-3' structures is mostly driven by the large gas cavities acting on the following blades. From this result it follows that in order to correctly predict the RPD when '3-3' cavity structures are expected the alternating pattern of the cavity must be captured by the model. To study the effect of the gas cavities on the liquid pumped by the blades, the local liquid flux, obtained by multiplying the liquid velocity by the liquid volume fraction, on a plane just above the upper part of the impeller disk was analyzed and it is reported in Figure 15 for the single phase case, Case I and Case III. Figure 15a shows that the liquid is drawn towards the impeller from the low-pressure zone close to the shaft, it then enters the space between two blades (vane) where it is radially accelerated by the rotating motion of the impeller. As the gas cavities develop, Figure 15b, the vane space available for the passage of liquid is reduced, limiting the pumping capacities of the impeller. This phenomenon leads to a lower liquid
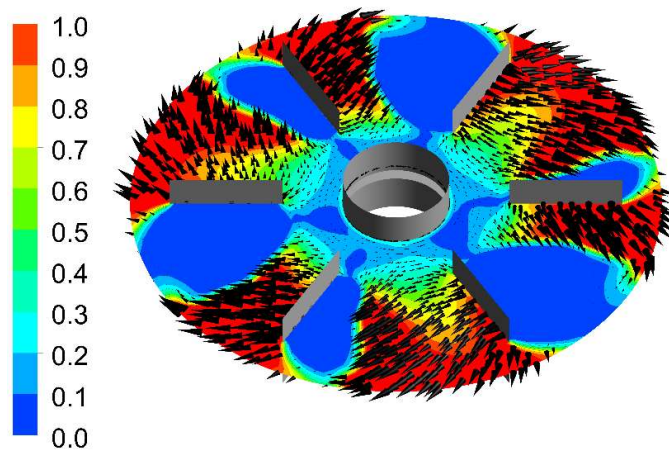
22

flux entrained from the low-pressure zone close to the shaft, as can be observed by the larger blue zone corresponding to a lower liquid flux.

(a)

(b)
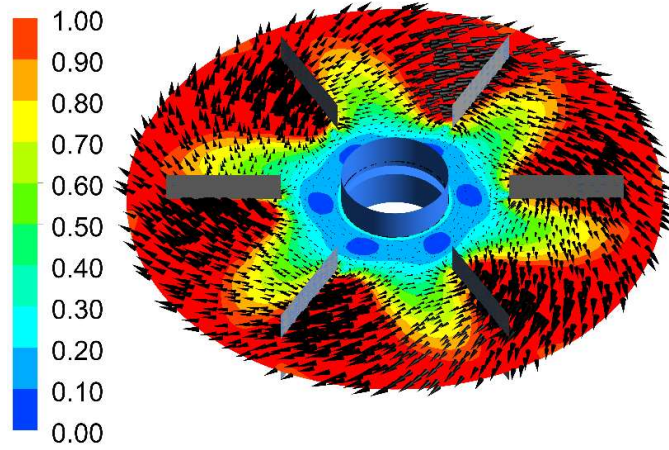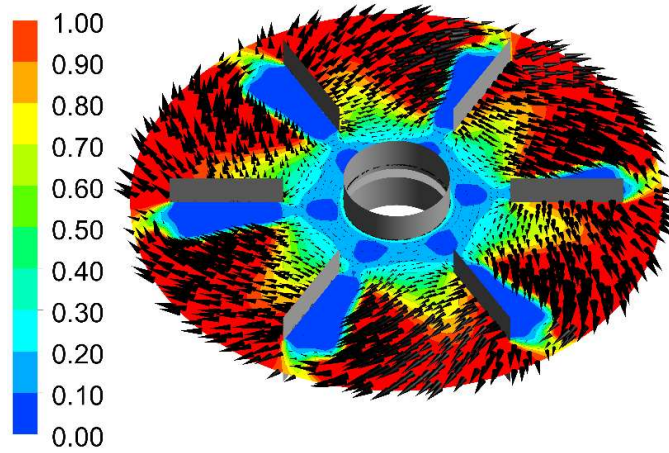
Figure 15 – Liquid flux on a plane above the impeller disk in single phase conditions (a) and for Cases I (b) and III (c). The color map shows the flux norm in m/s.

With the increase of the gas cavity size, the vane space available for the passage of liquid is further reduced, the liquid drawn towards the impeller consequently significantly decreases, leading to very small fluxes being entrained by the low-pressure zone close to the shaft. The low fluxes zones eventually rearrange to the characteristic pattern observable in Figure 15c, in which sections of the disk between two blades where a large cavity is present have lowered liquid fluxes while in the following and preceding sections the flux is weakly increased, since liquid flux is diverted towards them from the bordering section. The different liquid flux treated by the vanes leads to the formation of asymmetrical cavities, namely where the liquid flux is lower large cavities develop while the increased liquid flux produces small cavities. A similar behavior was observed in centrifugal pumps, in which the phenomenon of rotating cavitation was analyzed [40]. It is worth observing that the origin of the asymmetrical cavities is not related to the periodicity of the flow field due to the change of the relative position of baffles and blades over time, for this reason the transient solution of the RANS equations is not required for correctly predicting the 3-3 cavity regime.

6   Conclusions

In this work the formation of gas cavities behind the Rushton impeller blades and the subsequent relative power demand at different inlet gas-flow rates in a gas-liquid stirred tank were studied by means of CFD simulations. The system was studied in the loading flow regime in which either vortex-clinging or small '3-3' cavity structures develop.

The predicted cavity area and the gassed to ungassed power ratio were compared with experimental data from the literature. The study highlighted that the RANS-TFM approach, in which a single bubble diameter obtained from established published correlations was assumed, is successful in reproducing the main features of the flow, provided that the bubble diameter in the impeller zone is used.

For the first time the formation of clinging and small '3-3' cavity structures, both in terms of shape and dimension of the gas cavities are predicted with a steady multiple reference frame approach. The decrease of the power drawn by the impeller is also predicted and the numerical

24

results showed a very good agreement with the experimental data. The formation of vortex cavities cannot be predicted by the model, most likely due to the impossibility of the Reynolds Averaged formulation of the Navier-Stokes equations to predict the formation of the trailing vortexes behind the impeller blades.

The analysis of the pressure field on the impeller blades showed that the power reduction observed with the formation of gas cavities is mostly due to the decrease of the pressure on the front face of the blades. An original interpretation of the mechanism of formation of the small '3-3' cavities is proposed, locally analyzing the reduced pumping capacity of the impeller due to the growth of gas cavities, leading to a consequent pressure decrease that is higher on the blades following a large cavity, since the gas phase obstructs the liquid flow.

[1]   D.A. Brown, P. Jones, J.C. Middleton, G. Papadopoulos, E.B. Arik, Experimental methods, in: E.L. Paul, V.A. Atiemo-Obeng, S.M. Kresta (Eds.), Handb. Ind. Mix. Sci. Pract., John Wiley & Sons Inc., Hoboken, New Jersey, 2004: pp. 145--256.

[2]   E. Kadic, T.J. Heindel, An Introduction to Bioreactor Hydrodynamics and Gas-Liquid Mass Transfer, John Wiley & Sons, Inc., Hoboken, NJ, USA, 2014. https://doi.org/10.1002/9781118869703.

[3]   M. Liu, CFD Modeling of Stirred Tank Reactors, in: S.M. Kresta, A.W. Etchells III, V.A. Atiemo-Obeng, D.S. Dickey (Eds.), Adv. Ind. Mix. a Companion to Handb. Ind. Mix., John Wiley & Sons, Ltd., 2016: pp. 123–148.

[4]   V. Cappello, C. Plais, C. Vial, F. Augier, Scale-up of aerated bioreactors: CFD validation and application to the enzyme production by Trichoderma reesei, Chem. Eng. Sci. 229 (2021) 116033. https://doi.org/10.1016/j.ces.2020.116033.

[5]   P. Shi, R. Rzehak, Bubbly flow in stirred tanks: Euler-Euler/RANS modeling, Chem. Eng. Sci. 190 (2018) 419–435. https://doi.org/10.1016/j.ces.2018.06.001.

[6]   R. Rzehak, E. Krepper, Closure models for turbulent bubbly flows: A CFD study, Nucl. Eng. Des. 265 (2013) 701–711. https://doi.org/10.1016/j.nucengdes.2013.09.003.

[7]   A.D. Gosman, C. Lekakou, S. Politis, R.I. Issa, M.K. Looney, Multidimensional modeling of turbulent two-phase flows in stirred vessels, AIChE J. 38 (1992) 1946–1956. https://doi.org/10.1002/aic.690381210.

[8]   G. Montante, D. Horn, A. Paglianti, Gas–liquid flow and bubble size distribution in stirred tanks, Chem. Eng. Sci. 63 (2008) 2107–2118. https://doi.org/10.1016/j.ces.2008.01.005.

[9]   G.L. Lane, M.P. Schwarz, G.M. Evans, Numerical modelling of gas–liquid flow in stirred tanks, Chem. Eng. Sci. 60 (2005) 2203–2214. https://doi.org/10.1016/j.ces.2004.11.046.

[10]   A. Buffo, M. Vanni, D.L. Marchisio, Multidimensional population balance model for the simulation of turbulent gas–liquid systems in stirred tank reactors, Chem. Eng. Sci. 70 (2012) 31–44. https://doi.org/10.1016/j.ces.2011.04.042.

[11]   M. Jahoda, L. Tomášková, M. Moštěk, CFD prediction of liquid homogenisation in a gas–liquid stirred tank, Chem. Eng. Res. Des. 87 (2009) 460–467.

https://doi.org/10.1016/j.cherd.2008.12.006.

[12] J. Gimbun, C.D. Rielly, Z.K. Nagy, Modelling of mass transfer in gas–liquid stirred tanks agitated by Rushton turbine and CD-6 impeller: A scale-up study, Chem. Eng. Res. Des. 87 (2009) 437–451. https://doi.org/10.1016/j.cherd.2008.12.017.

[13] F. Maluta, A. Paglianti, G. Montante, Modelling of biohydrogen production in stirred fermenters by Computational Fluid Dynamics, Process Saf. Environ. Prot. 125 (2019) 342–357. https://doi.org/10.1016/j.psep.2018.09.020.

[14] M.M.C.G. Warmoeskerken, J. Feijen, J.M. Smith, Hydrodynamics and power consumption in stirred gas-liquid dispersions., in: FLUID Mix. Symp., Institution of Chemical Engineers, BRADFORD, U.K., 1981: pp. J1-B14.

[15] A.W. Nienow, Gas dispersion performance in fermenter operation, Chem. Eng. Prog. 86 (1990) 61–71.

[16] A.W. Nienow, M.M.C.G. Warmoeskerken, J.M. Smith, M. Konno, On the flooding/loading transition and the complete dispersal condition in aerated vessels agitated by a Rushton-turbine, in: Proc. 5th Eur. Conf. Mix., BHRA Fluid Engineering, Wurzburg, Germany, 1985: pp. 143–154.

[17] V.V. Ranade, M. Perrard, C. Xuereb, N. Le Sauze, J. Bertrand, Influence of Gas Flow Rate on the Structure of Trailing Vortices of a Rushton Turbine: PIV Measurements and CFD Simulations, Chem. Eng. Res. Des. 79 (2001) 957–964. https://doi.org/10.1205/02638760152721190.

[18] F. Kerdouss, A. Bannari, P. Proulx, CFD modeling of gas dispersion and bubble size in a double turbine stirred tank, Chem. Eng. Sci. 61 (2006) 3313–3322. https://doi.org/10.1016/j.ces.2005.11.061.

[19] A.R. Khopkar, A.R. Rammohan, V.V. Ranade, M.P. Dudukovic, Gas–liquid flow generated by a Rushton turbine in stirred vessel: CARPT/CT measurements and CFD simulations, Chem. Eng. Sci. 60 (2005) 2215–2229. https://doi.org/10.1016/j.ces.2004.11.044.

[20] A.R. Khopkar, P.A. Tanguy, CFD simulation of gas–liquid flows in stirred vessel equipped with dual rushton turbines: influence of parallel, merging and diverging flow configurations, Chem. Eng. Sci. 63 (2008) 3810–3820. https://doi.org/10.1016/j.ces.2008.04.039.

[21] S.S. Kshatriya, A.W. Patwardhan, A. Eaglesham, Experimental and CFD Characterization of Gas Dispersing Asymmetric Parabolic Blade Impellers, Int. J. Chem. React. Eng. 5 (2007). https://doi.org/10.2202/1542-6580.1381.

[22] N.G. Deen, T. Solberg, B.H. Hjertager, Flow Generated by an Aerated Rushton Impeller: Two-phase PIV Experiments and Numerical Simulations, Can. J. Chem. Eng. 80 (2002) 1–15. https://doi.org/10.1002/cjce.5450800406.

[23] M. Simonnet, C. Gentric, E. Olmos, N. Midoux, Experimental determination of the drag coefficient in a swarm of bubbles, Chem. Eng. Sci. 62 (2007) 858–866. https://doi.org/10.1016/j.ces.2006.10.012.

[24] M. Simonnet, C. Gentric, E. Olmos, N. Midoux, CFD simulation of the flow field in a bubble column reactor: Importance of the drag force formulation to describe regime transitions, Chem. Eng. Process. Process Intensif. 47 (2008) 1726–1737. https://doi.org/10.1016/j.cep.2007.08.015.

[25] F. Maluta, A. Paglianti, G. Montante, Two-fluids RANS predictions of gas cavities, power consumption, mixing time and oxygen transfer rate in an aerated fermenter scale-down stirred with multiple impellers, Biochem. Eng. J. 166 (2021) 107867. https://doi.org/10.1016/j.bej.2020.107867.

[26] A. Paglianti, M. Fujasova, G. Montante, A simple model for power consumption in gassed and boiling stirred vessels, AIChE J. 54 (2008) 646–656. https://doi.org/10.1002/aic.11414.

[27] A.W. Nienow, J.J. Ulbrecht, Gas-liquid mixing in high viscosity systems, in: J.J. Ulbrecht, G.K. Patterson (Eds.), Mix. Liq. by Mech. Agit., Gordons and Breach, New York, 1985: pp. 203–235.

[28] A.W. Nienow, D.J. Wisdom, J.C. Middleton, The effect of scale and geometry on flooding, recirculation, and power in gassed stirred vessels, in: Proc. 2nd Eur. Conf. Mix., BHRA Fluid Engineering, Mons, BE, 1977: pp. F1-1-F1-16.

[29] J.M. Smith, M.M.C.G. Warmoeskerken, E. Zeef, Flow conditions in vessels dispersing gases in liquids with multiple impellers, in: C.S. Ho, J.Y. Oldshue (Eds.), Biotechnol. Process. Scale-up Mix., American Institute of Chemical Engineers, New York, 1987: pp. 107–115.

[30] A.D. Burns, T. Frank, I. Hamill, J.-M.M. Shi, The Favre Averaged Drag Model for Turbulent Dispersion in Eulerian Multi-Phase Flows, in: Fifth Int. Conf. Multiph. Flow, ICMF-2004, Yokohama, Japan, 2004: pp. 1–17.

[31] F. Scargiali, A. D'Orazio, F. Grisafi, A. Brucato, Modelling and Simulation of Gas–Liquid Hydrodynamics in Mechanically Stirred Tanks, Chem. Eng. Res. Des. 85 (2007) 637–646. https://doi.org/10.1205/cherd06243.

[32] R. Clift, J.R. Grace, M.E. Weber, Bubbles, drops, and particles, 1st ed., Dover Publications, Inc., Mineola, New York, 2005.

[33] S.S. Alves, C.I. Maia, J.M.T. Vasconcelos, A.J. Serralheiro, Bubble size in aerated stirred tanks, Chem. Eng. J. 89 (2002) 109–117. https://doi.org/10.1016/S1385-8947(02)00008-6.

[34] L. Schiller, A. Naumann, Über die grundlegenden berechnungen bei der schwerkraftbereitung, Zeitschrift Des Vereines Dtsch. Fngenieure. 77 (1933) 318--321.

[35] M. Coroneo, G. Montante, A. Paglianti, F. Magelli, CFD prediction of fluid flow and mixing in stirred tanks: Numerical issues about the RANS simulations, Comput. Chem. Eng. 35 (2011) 1959–1968. https://doi.org/10.1016/j.compchemeng.2010.12.007.

[36] H.. Versteeg, W. Malalasekera, An Introduction to Computational Fluid Dynamics - The Finite Volume Method, 2nd ed., Pearson Education Limited, Harlow, England (UK), 2007.

[37] K. van't Riet, J.M. Smith, The behaviour of gas—liquid mixtures near Rushton turbine blades, Chem. Eng. Sci. 28 (1973) 1031–1037. https://doi.org/10.1016/0009-2509(73)80005-3.

[38] M.M.C.G. Warmoeskerken, Gas-liquid dispersing characteristics of turbine agitators, TU Delft, 1986.

[39] J.C. Middleton, J.M. Smith, Gas-liquid mixing in turbulent systems, in: E.L. Paul, V.A. Atiemo-Obeng, S.M. Kresta (Eds.), Handb. Ind. Mix. Sci. Pract., John Wiley & Sons Inc., Hoboken, New Jersey, 2004: pp. 585–638.

[40] J. Friedrichs, G. Kosyna, Rotating Cavitation in a Centrifugal Pump Impeller of Low Specific Speed, J. Fluids Eng. 124 (2002) 356–362. https://doi.org/10.1115/1.1457451.